Natural Resources Canada | Ressources naturelles Canada

GEOLOGICAL SURVEY OF CANADA
OPEN FILE 8925

Mapping tectonic stress at subduction zones with earthquake focal mechanisms: application to Cascadia, Japan, Nankai, Mexico, and northern Chile

A.P. Plourde and J.F. Cassidy

2022

Canada

ISSN 2816-7155
ISBN 978-0-660-45736-9
Catalogue No. M183-2/8925E-PDF

GEOLOGICAL SURVEY OF CANADA
OPEN FILE 8925

Mapping tectonic stress at subduction zones with earthquake focal mechanisms: application to Cascadia, Japan, Nankai, Mexico, and northern Chile

A.P. Plourde and J.F. Cassidy

2022

Permanent link: https://doi.org/10.4095/330943

This publication is available for free download through GEOSCAN (https://geoscan.nrcan.gc.ca/).

Recommended citation
Plourde, A.P. and Cassidy, J.F., 2022. Mapping tectonic stress at subduction zones with earthquake focal mechanisms: application to Cascadia, Japan, Nankai, Mexico, and northern Chile; Geological Survey of Canada, Open File 8925, 1 .zip file. https://doi.org/10.4095/330943

Publications in this series have not been edited; they are released as submitted by the author.

Table of Contents

Abstract

Earthquake focal mechanisms have contributed substantially to our understanding of modern tectonic stress regimes, perhaps more than any other data source. Studies generally group focal mechanisms by epicentral location to examine variations in stress across a region. However, stress variations with depth have rarely been considered, either due to data limitations or because they were believed to be negligible. This study presents 3D grids of tectonic stress tensors using existing focal mechanism catalogs from several subduction zones, including Cascadia, Japan, Nankai, Mexico, and northern Chile. We bin data into 50 x 50 x 10 km cells (north, east, vertical), with 50% overlap in all three directions. This resulted in 181380 stress inversions, with 90% of these in Japan (including Nankai). To the best of our knowledge, this is the first examination of stress changes with depth in several of these regions. The resulting maps and cross-sections of stress can help distinguish locked and creeping segments of the plate interface. Similarly, by dividing the focal mechanism catalog in northern Japan into those before and those >6 months after the 2011 M_W 9.1 Tohoku-Oki earthquake, we are able to produce detailed 3D maps of stress rotation, which is close to 90° near the areas of highest slip. These results could inform geodynamic rupture models of future megathrust earthquakes in order to more accurately estimate slip, shaking, and seismic hazard. Southern Cascadia and Nankai appear to have sharp stress discontinuities at ∼20 km depth, and northern Cascadia may have a similar discontinuity at ∼30 km depth. These stress boundaries may relate to rheological discontinuities in the forearc, and may help us unravel how forearc composition influences subduction zone behaviour and seismic hazard.

1 Introduction

Stress tensor estimates derived from earthquake focal mechanisms have formed a crucial asset to our understanding of tectonic processes. They have often appeared to reflect processes independent from those observed in GPS-derived strain tensors (*Balfour et al.*, 2011) or direct, borehole stress estimates (*Mazzotti and Townend*, 2010), leading to a more complex, but richer, tectonic analysis. To date, relatively sparse catalogs of focal mechanism estimates have led most investigators to either estimate a single tensor for entire, broad seismic zones (e.g. *Mazzotti and Townend*, 2010) or to estimate stress tensors for targeted clusters of earthquakes (e.g. *Balfour et al.*, 2011). Variation of tectonic stress with depth is rarely considered in such studies, in part because of reports that it is usually insignificant (*Heidbach et al.*, 2018). Exceptions include investigations of the Japan subduction zone by *Terakawa and Matsu'ura* (2010) and *Yang et al.* (2013), who binned focal mechanisms into regular 3D grids. In this study we adopt a similar approach of binning focal mechanisms based on a regular 3D grid, and apply it to multiple subduction zones, including Cascadia and those in Japan. Using a consistent method of binning data, as well as for inverting and displaying stress tensor estimates, facilitates meaningful comparisons between regions. For several of the regions, to the best of our knowledge, this is also the first examination of stress changes with depth.

Only a small subset of the stress tensor results are included in this report, where they are plotted in map and cross-section figures. The full set of stress inversion results appears in Table S1, as well as in map and cross-section figures, in the supplementary information. Some of the focal mechanism data used in this study was accessed via the International Seismological Centre (ISC) Bulletin (*Lentas et al.*, 2019), accessed at http://www.isc.ac.uk/iscbulletin/search/fmechanisms/. These include contributions from the Global Centroid Moment Tensor catalog (*Dziewonski et al.*, 1981; *Ekström et al.*, 2012), as well as a variety of other agencies that will not be listed here. As not all publicly available focal mechanism catalogs are uploaded to the ISC, catalogs accessed elsewhere that were used in this study are described in Table 1.

2 Methods

2.1 Stress Inversion

We estimate the state of tectonic stress from earthquake focal mechanisms using the procedure of *Plourde and Nedimović* (2021), which is similar to those of *Vavryčuk* (2014) and *Plourde and Bostock* (2019). We account for uncertainty in the focal mechanisms by repeating each stress inversion 1000 times, each time producing a new noise realization by perturbing the focal mechanisms with a random rotation. The

Table 1. List of focal mechanism catalogs use in this study, divided by region. Note that the sources listed are in addition to those accessed via the ISC Bulletin (*Lentas et al.*, 2019). N_{FM} indicates the total number unique earthquakes with a focal mechanism for the region, from all sources; it only includes events that lie within the map bounds of the figures shown in Section 3, and in the cases of Cascadia and Japan separate N_{FM} are given for each of the two map areas.

Region	**Data sources (in addition to the ISC Bulletin)**	**N_{FM}**
Cascadia	i) Geological Survey of Canada catalog, including the data of *Balfour et al.* (2011) and unpublished mechanisms. ii) Northern California Earthquake Data Center (NCEDC). Accessed via the ObsPy (Python) package LibComCat: https://github.com/usgs/libcomcat	6740 (N. Cascadia) 4626 (S. Cascadia)
Japan	i) (Japan) National Research Institute for Earth Science and Disaster Resilience (NIED) earthquake mechanism catalog: https://www.fnet.bosai.go.jp/event/search.php?LANG=en. ii) *Uchide* (2020)	102598 (N. Japan) 62505 (S. Japan)
Mexico	*Franco et al.* (2020), National Autonomous University of Mexico (UNAM) http://132.248.6.13/∼cmt/	2565
Chile	*Herrera et al.* (2021)	2346

absolute angles of rotation for each earthquake are drawn from Laplace distributions scaled according to the estimated standard error assigned their focal mechanisms. However, most focal mechanism catalogs do not supply error estimates, so in these cases we assume a standard error of 30°. The output stress tensor estimate is computed by taking a mean of the results from each realization.

Within each realization, stress is estimated using an iterative method based on the linear stress inversion of *Michael* (1984). The purpose of iterations is simply to select which of the two nodal planes is most likely to be the true fault plane. Whereas *Vavryčuk* (2014) selected the fault plane that was least stable, i.e. had the highest instability factor I in the current stress tensor estimate, we combine the instability and slip angle methods (*Lund and Slunga*, 1999) by selecting fault planes that maximize:

$$\max \quad (\overrightarrow{v_{\mathrm{pre}}} \cdot \overrightarrow{v_{\mathrm{obs}}})\, I, \tag{1}$$

where $\overrightarrow{v_{\mathrm{pre}}}$ and $\overrightarrow{v_{\mathrm{obs}}}$ are the predicted and observed slip directions. This formulation favors nodal planes that, given the current stress estimate, are 1) well oriented for slip according to Mohr-Coulomb failure criterion, and 2) have a rake angle consistent with the predicted sense of shear.

Stress tensors are expressed with principal stress axis directions $\overrightarrow{\sigma_i}$ and a shape ratio R, defined as:

$$R = \frac{\sigma_1 - \sigma_2}{\sigma_1 - \sigma_3}, \tag{2}$$

such that a value of $R = 0$ indicates uniaxial tension and $R = 1$ indicates uniaxial compression. Note that in this section we use the scalar σ_i to refer to (relative) stress values and the vector $\overrightarrow{\sigma_i}$ to refer to the axis directions, but in later sections we will use unaccented σ_i more casually to refer to both the value and direction. Although the stress inversion method can provide detailed probability distributions for $\overrightarrow{\sigma_i}$ and R, there is no practical way to express the full distribution for large numbers of inversions. Instead, we first reduce the uncertainty on each axis to a 90% confidence angle u_i and record the 90% confidence limits on R. We can then estimate an overall uncertainty angle (U) of the stress tensors, at the 90% confidence level, as:

$$U = Ru_1 + (1 - R)u_3. \tag{3}$$

The dependence of U on R arises from the fact that for uniaxial compression, $\overrightarrow{\sigma_2}$ and $\overrightarrow{\sigma_3}$ become arbitrary, and (vice-versa) $\overrightarrow{\sigma_1}$ and $\overrightarrow{\sigma_2}$ become arbitrary for uniaxial tension. Therefore, as $R \to 1$ uncertainties u_2 and u_3 will naturally increase (or, as $R \to 0$, u_1 and u_2 will naturally increase), but those increases do not suggest a higher level of overall uncertainty.

2.2 Grid and Plotting

For each region, we define a grid with 25 km spacing in the east–west and north–south horizontal directions, and 5 km spacing in depth. The grid is always locally cartesian, i.e. it is not distorted by the choice of map projection. We estimate the stress tensor at each grid-point with $\geq$10 focal mechanisms in its 50 x 50 x 10 km bin; note that the bin size results in 50% spatial overlap with adjacent points in all direction. We represent stress on two maps per region, per depth interval: one for σ_1 and one for σ_3. The symbol used to represent each stress axis depends on its plunge angle θ:

- For near-horizontal axes ($0 \leq \theta < 20°$): the axis trend φ is plotted as a line, with its relative length scaled according to $\cos^2\theta$.
- For intermediate-plunge axes ($20 \leq \theta \leq 70°$): φ is plotted as a above, but with an arrowhead in the plunge direction. A circle, with relative scale determined by $\sin^2\theta$, is additionally plotted.
- For near-vertical axes ($70 < \theta \leq 90°$): Only the circle, with relative scale determined by $\sin^2\theta$, is plotted; φ is not represented.

The σ_1 symbols are colored according to their shape ratio R, and the σ_3 symbols are colored according to their uncertainty angle U. To produce cross-sections of stress, new grid points are placed at 25 km horizontal spacing along the section, and their stress tensor is estimated using nearby stress inversions. Only stress tensors from the same depth and <25 km horizontal distance are used; contributing tensors are weighted according to both the inverse horizontal distance from the new grid point and their respective uncertainties. The symbols used to plot stress are equivalent to those on map figures except rotated relative to the vertical plane of the cross-section, such that the effective plunge-direction is pointing into the page.

3 Results

This section displays subsets of the stress inversions from each region in maps and cross-sections. All map figures show the trench as a thick green line, as well as the 20, 40, 60, 80, and 100 km plate interface contours as thin green lines, with all plate-interface models corresponding to those in the Slab2 collection (*Hayes et al.*, 2018). A full set of maps—including all depths at which stress was inverted in a particular region—is contained in the supplementary folders to this report. All stress inversions are additionally described in Table S1, which includes the following information for each inversion:

- Latitude, longitude, depth, and the number of focal mechanisms.
- Trend, plunge, and uncertainty angles for each axis (φ_i, θ_i, and u_i).
- R and its 90% confidence limits. Note that the R reported comes from the reported stress tensor, which is the mean result of the 1000 iterations, whereas the confidence limits are the 5$^{\text{th}}$ and 95$^{\text{th}}$ percentiles of R from the individual iterations, so in rare cases the reported R actually falls outside the confidence limits.
- Uncertainty (U) as defined by Eq. 3.
- Diversity, defined as the mean Kagan rotation angle (*Kagan*, 2007) of the input focal mechanisms away from the average focal mechanism. The average focal mechanism is defined as the double-couple component of the mean of the unit moment tensors corresponding to each focal mechanism.
- Misfit, defined as the mean angle between the predicted and observed slip vectors.

A summary of characteristic uncertainty, diversity, and misfit angles from each subduction zone is presented in Table 2. Sufficient diversity is essential to achieve reliable stress inversions, although a high

measured diversity can reflect low data quality in addition to true diversity of fault orientations. We can attempt to qualitatively interpret data quality from the diversity/misfit ratio; for example, Chile has a relatively high diversity/misfit ratio (37.1/23.8 = 1.56, 50^{th} percentiles from Table 2) so we interpret its focal mechanisms to be more reliable on average than those of Mexico, or Northern or Southern Cascadia that have the lowest diversity/misfit ratios. High diversity paired with high misfit may indicate lower data quality than low diversity with low misfit (even with similar diversity/misfit ratios), but it could also be indicative of actual spatiotemporal stress variations within individual inversions. With enough data, it is possible to have low uncertainty on the (mean) stress tensor even if diversity and misfit are high.

Japan (including Nankai) has most of the lowest-uncertainty stress inversions (comparing 5^{th} percentiles, Table 2) owing to extremely dense station coverage and a dense focal mechanism catalog onshore. However, because northern Japan also has many inversions offshore where data quality is much lower, its median uncertainties are similar to those in Cascadia. Far offshore regions have poor azimuthal coverage (from onshore seismometers) and are also impacted by focal depth uncertainties which likely blur stress estimates over $\pm$20 km depth. Hypocenter uncertainty is not explicitly accounted for in our estimates of stress uncertainty, therefore offshore estimates of stress uncertainty could be artificially low. This issue is least prominent in Japan because it has had the most significant ocean-bottom seismometer coverage of its offshore, but even in Japan there is a substantial gap in focal depth and mechanism quality between on- and offshore. Mexico has the highest average uncertainties, probably in part because the majority of its inversions are offshore; however, it also has relatively low diversities and misfits, indicating that a true lack of fault diversity is hindering precise stress estimates.

Table 2. General statistics of stress inversions from each region, including the number of stress inversions N, and the 5^{th}, 50^{th}, and 95^{th} percentile of their uncertainties, diversities, and misfits.

	N	Uncertainty (°)			Diversity (°)			Misfit (°)		
		5^{th}	50^{th}	95^{th}	5^{th}	50^{th}	95^{th}	5^{th}	50^{th}	95^{th}
Northern Cascadia	705	6.5	18.8	37.8	45.6	56.5	68.4	25.4	44.8	62.6
Southern Cascadia	517	6.5	17.4	34.6	26.4	54.1	67.1	16.3	39.3	56.9
Chile	331	8.6	18.4	31.2	14.3	37.1	59.8	6.8	23.8	45.0
Nankai	2305	2.8	12.8	30.8	22.7	40.0	56.7	13.1	25.6	46.0
Janan (Full)	4879	4.1	15.9	35.8	19.0	42.8	62.2	10.6	30.7	57.1
Japan (Pre)	2801	5.6	18.9	36.0	16.0	39.7	59.1	8.7	27.7	49.7
Japan (Post)	2999	4.4	17.5	36.7	16.4	41.1	60.4	9.8	28.0	51.8
Mexico	398	9.4	22.7	41.6	14.8	28.8	48.7	9.5	23.5	52.3

3.1 Northern Cascadia

Pressure and tension axes from a subset of focal mechanisms in the 0–10 km depth interval are plotted in Figure 1. In some areas of dense seismicity, it is difficult to visually interpret dominant stress orientation because there is high degree of scatter in their azimuths—note that northern Cascadia was the region with the highest average diversity (Table 2). Figure 2 displays stress inversion results for the shallowest 20 km. Results are generally consistent with those of *Balfour et al.* (2011), who observed σ_1 and maximum horizontal stress directions to be trench-normal above the western (shallow, locked) portion of the megathrust and trench-parallel in the eastern forearc. As there are few earthquakes in the western (near-trench) forearc, the minimum event requirements of this study result in only one location where trench-normal σ_1 is resolved—along the coast of Vancouver island (10 to 20 km depth), which are our westernmost inversions. Our results extend further south and east than those of *Balfour et al.* (2011), yet they see remarkably uniform trench-parallel compression, generally with high R (close to uniaxial compression), which further demonstrates that the northward push of the Oregon Block is dominating crustal stress in the region (*McCaffrey et al.*, 2013). σ_3 is most commonly vertical, but there is much greater heterogeneity in σ_3 than there is σ_1. Some of this heterogeneity, such as the E–W σ_3 axes near 46.7°N, 121.5°W correspond to well-resolved, strike-slip, low R regions indicating a stress regime closer to E–W extension. Other examples, such as the dipping axes near 48.5°N, 123.5°W correspond to inversions with both high R and high uncertainty, so it should be expected that their σ_3 directions are poorly resolved.

Stress axes along cross-sections A–G are displayed in Figure 3, providing a easier way to examine changes with depth. N–S compression dominates the forearc stress field up to ∼30 km depth across the entire region (at least where stress is resolved). Where there are slab earthquakes—mainly in Lines C, D, and E—the results are consistent with a slab-pull force and show along-dip σ_3, with σ_1 near-normal to the plate interface. However, there is significant variation of intraslab R and it is rarely close to uniaxial tension. The one area where a markedly different slab stress state is observed is on the western, updip portion of Lines C and D (just east of the shoreline), where there are east-dipping σ_1 axes and trench-parallel σ_3. This stress state may represent a transition zone between the shallow, locked zone and the deeper, low-coupling zone.

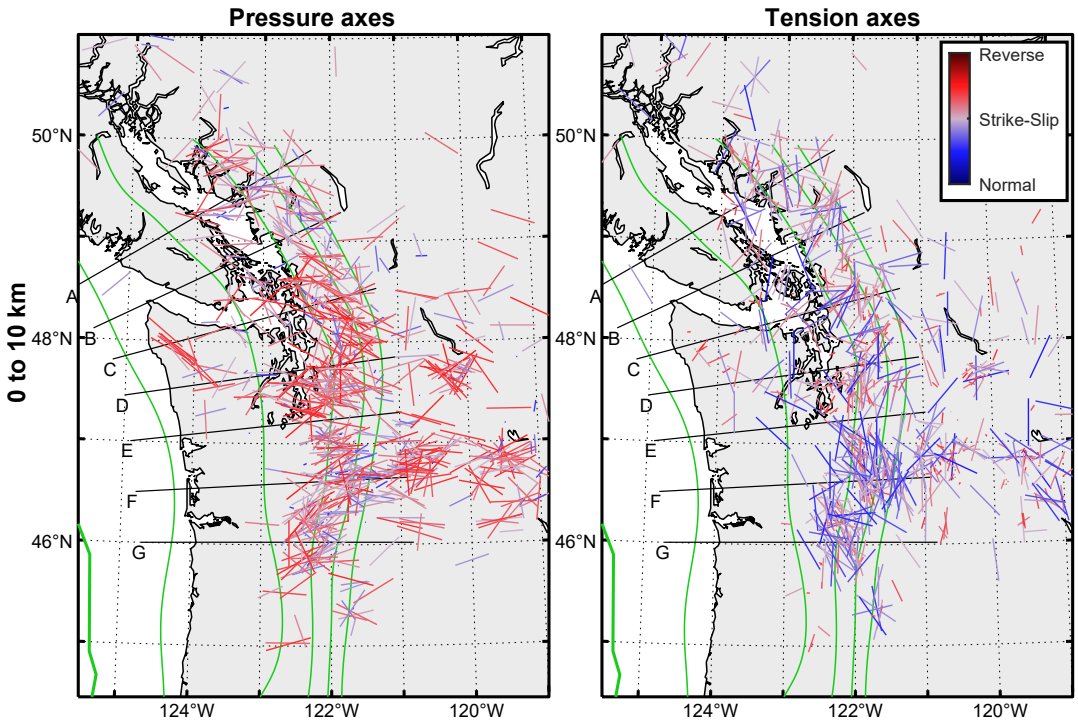

Figure 1. Pressure axes (left) and tension axes (right) from Northern Cascadia in the 0–10 km depth interval. Only 800 of 3016 total focal mechanisms from the depth range are shown; to make the axes be visually distinguishable, the mechanisms were culled with an iterative process based on distance to the 5$^{\text{th}}$-nearest focal mechanism. Axes are scaled according to $\cos^2\theta$, where θ is their plunge, and coloured by style of faulting. The thick green line indicates the trench, and the thin green lines indicate the 20, 40, 60, 80, and 100 km plate-interface contours of *Hayes et al.* (2018). Lines labeled A–G indicate cross-section locations, and are each 300 km long.

There appears to be a sharp transition with depth from the "forearc" stress state (N–S compression) to the main "slab" stress state (interface-normal σ_1, along-dip σ_3). There are some "slab" stress tensors plotted that are as much as 10 km shallower than the (*McCrory et al.*, 2012) plate interface model (Line C). These occur where the plate interface is >35 km depth and the two plates are thought to be only weakly coupled. It may be appealing to assume that the stress transition occurs at the plate interface and that the slab-like stress apparently in the deep forearc results from some combination of blurring due to the 10 km depth bins, uncertainty in focal depths, and uncertainty in the true interface depth. However, observations from other subduction zones (presented later in this report) suggest that a continuous stress regime across the plate interface is common downdip of the locked zone and thus favour a stress boundary within the forearc.

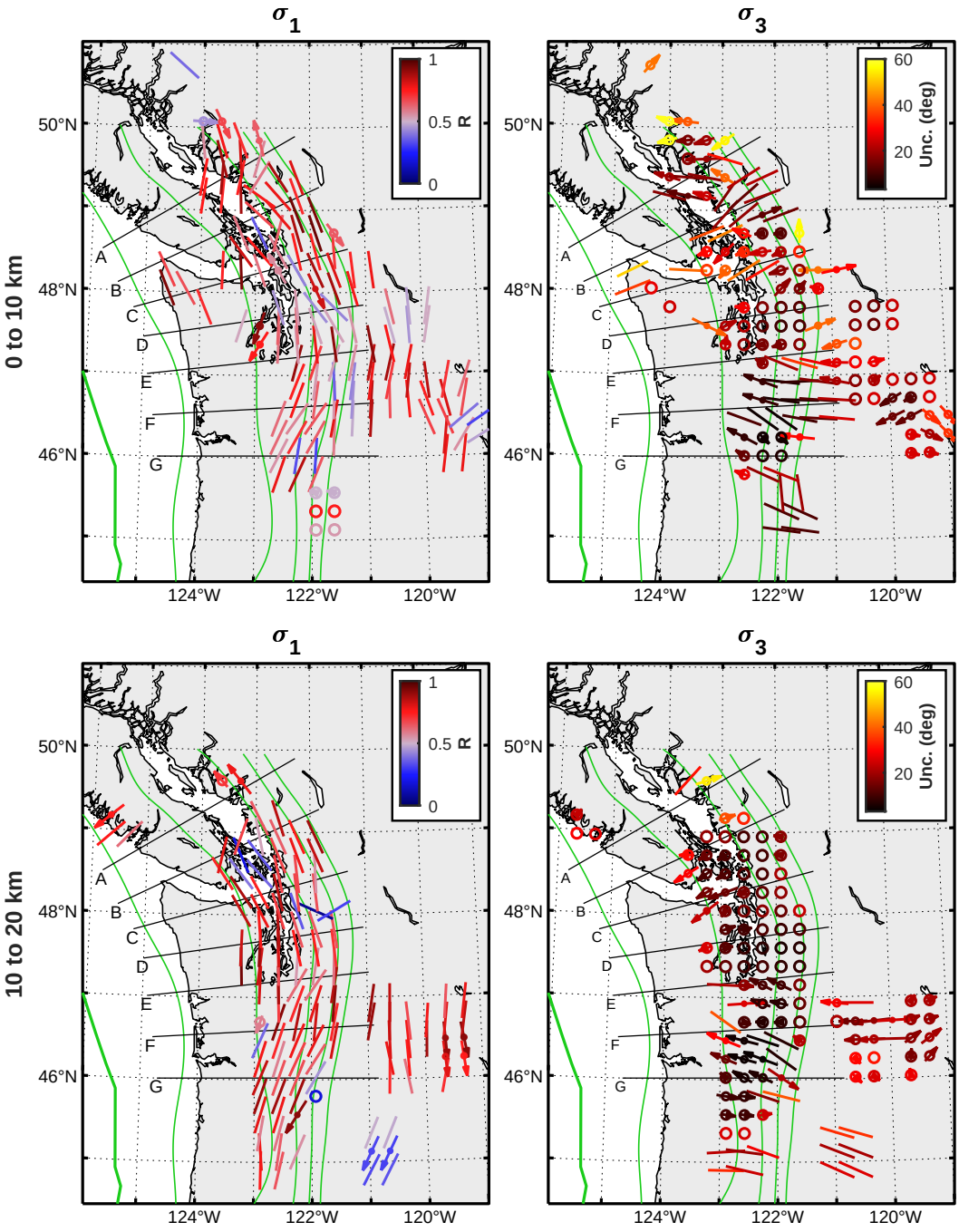

Figure 2. Stress inversion results from Northern Cascadia for the (top) 0–10 km and (bottom) 10–20 km depth ranges. The left panels show σ_1 axis orientation and are coloured according to R, right panels show σ_3 orientation and are coloured according to U. The symbols used to plot stress are described in Section 2.2. The thick green line indicates the trench, and the thin green lines indicate the 20, 40, 60, 80, and 100 km plate-interface contours of *Hayes et al.* (2018). Lines labeled A–G indicate cross-section locations, and are each 300 km long.

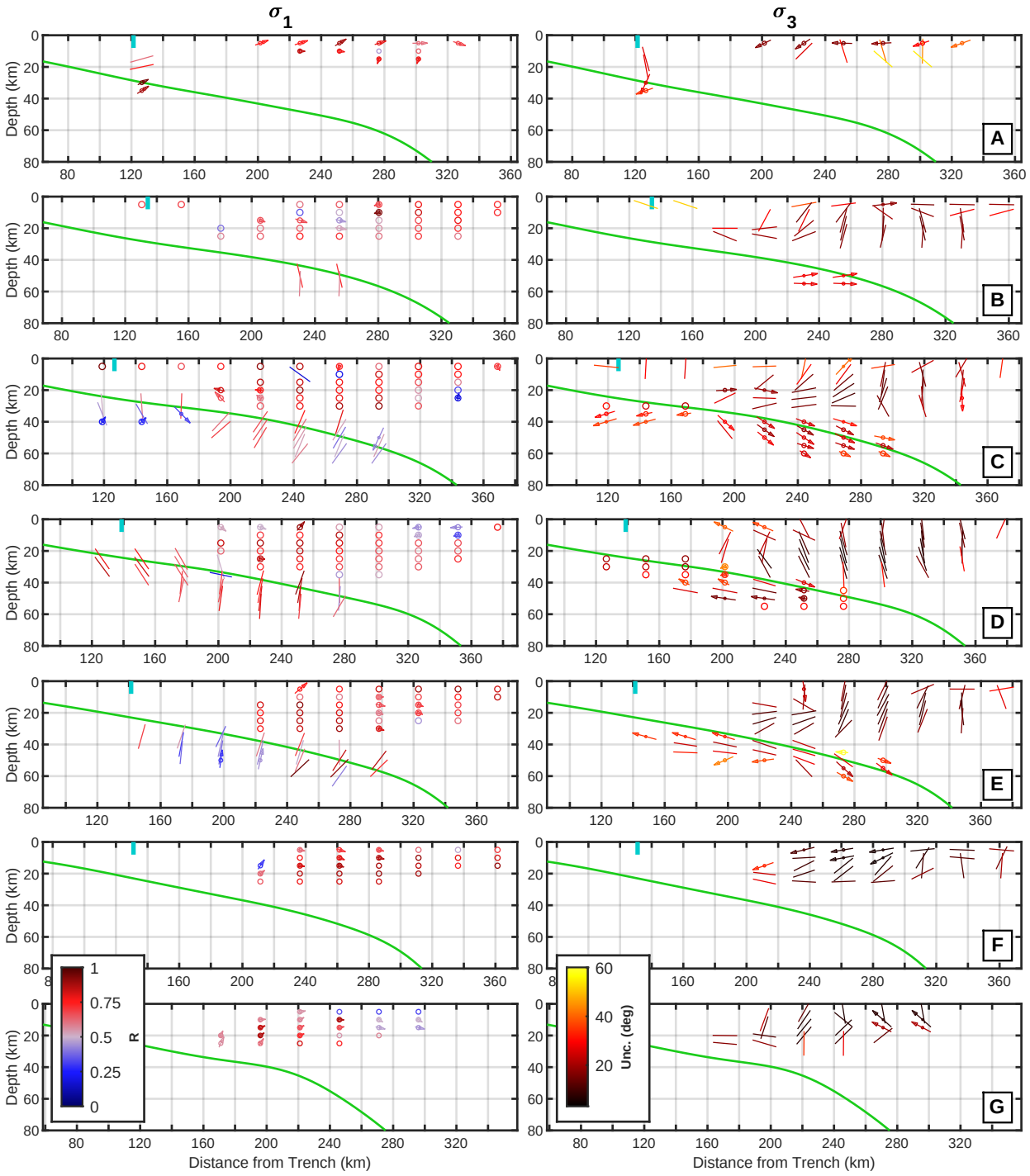

Figure 3. Cross-sections A–G of stress inversion results in Northern Cascadia. Positions of each section are indicated in Figure 1. Cyan markers at the surface indicate the position of the coastline in each section.

3.2 Southern Cascadia

The stress regime and distribution of seismicity in southern Cascadia both differ significantly from northern Cascadia. Earthquakes occur primarily near the very southern edge of the subduction zone, close to the Mendocino Triple Junction (MTJ) that connects Cascadia to the San Andreas Fault system, but on this southern edge they extend from the far offshore continuously eastward across the megathrust zone to the volcanic arc, or roughly above the 100 km plate interface contour, and beyond (Figure 4). The influence of the transform boundary to the south is apparent in the shallow crustal stresses, which are most commonly strike-slip with near N–S σ_1. *Wada et al.* (2010) suggested that the strong N–S compression results from the Pacific plate near the MTJ pushing northward against the subducting slab. R decreases eastward from the arc into the backarc, indicating relatively higher degrees of E–W extension, vs. N–S compression.

Cross-section views of stress along Lines A–D are displayed in Figure 5. *Li et al.* (2018) previously inverted for stress near Cape Mendocino in the slab and overriding plate independently, and they observed a stress discontinuity at the plate interface. We observe a stress rotation near the coastline in Line B that is consistent with their observations, supporting their notion that the interface is not strongly coupled in the region. This apparent stress contrast at the interface does not extend landward to interface-depths $>$20 km, where we mostly observe continuous stress regimes across the interface (although the stress regime differs from Line B to Line C). However, in these more landward forearc regions we do observe a significant rotation between the stress axes above and below a gap in seismicity, at $\sim$20 km depth. On Line B, σ_1 is approximately margin-normal in the shallow-forearc, but near-vertical (near-normal to the interface) in the slab and in the forearc just above the slab. On Line C, σ_1 is near-vertical in the shallow-forearc, but mostly margin-parallel just above (and in) the slab.

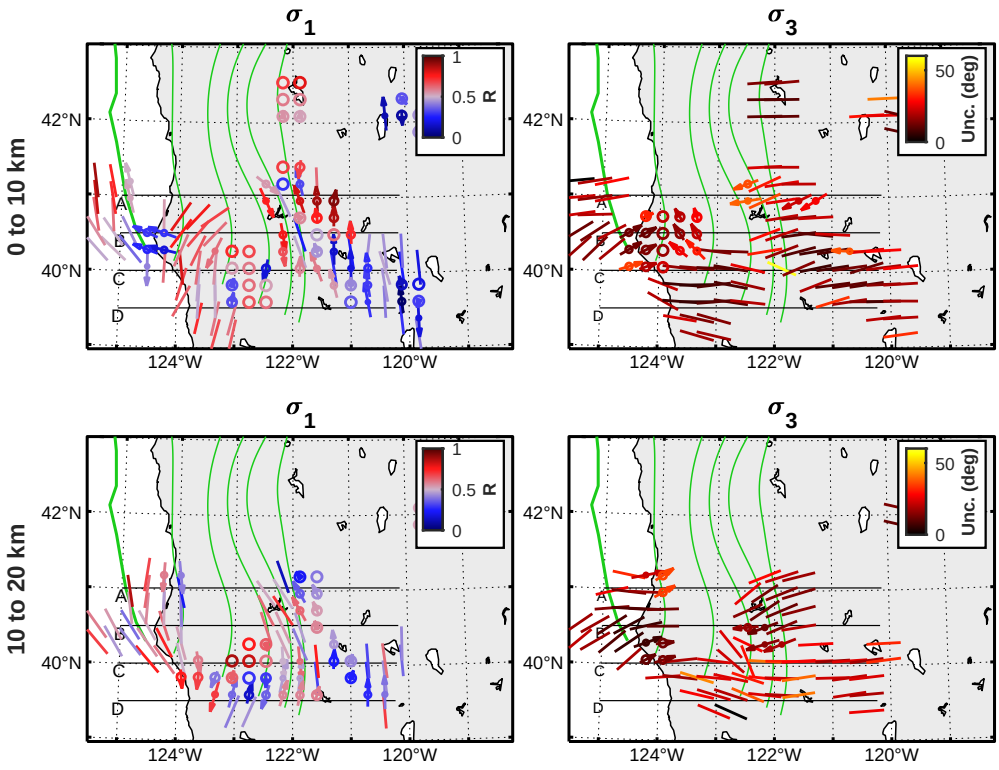

Figure 4. Stress inversion results from Southern Cascadia for the (top) 0–10 km and (bottom) 10–20 km depth ranges. The thick green line indicates the trench, and the thin green lines indicate the 20, 40, 60, 80, and 100 km plate-interface contours of *Hayes et al.* (2018). Lines labeled A–D indicate cross-section locations, and are each 410 km long.

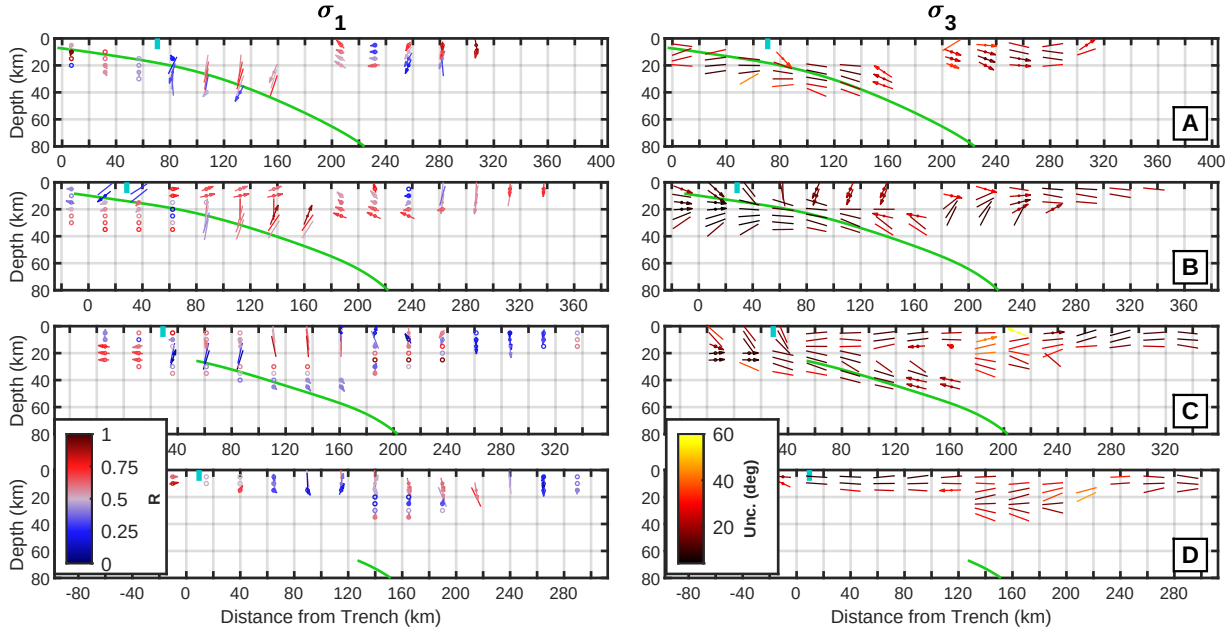

Figure 5. Cross-sections A–D of stress inversion results in Southern Cascadia. Positions of each section are indicated in Figure 4. Cyan markers at the surface indicate the position of the coastline in each section. Note that sections C and D do not intersect the trench, so the position of zero on their x-axes are arbitrary.

3.3 Northern Japan

Compared to Cascadia, Japan has both extremely abundant earthquakes and a dense network of seismometers, which have allowed detailed studies of its tectonic stress field (e.g. *Terakawa and Matsu'ura*, 2010; *Uchide*, 2020). Also, unlike other subduction zones discussed here, northern Japan has had a megathrust earthquake—the 2011 M_W 9.1 Tohoku-oki earthquake—recently enough to have significant seismic catalogs both before and after. Several studies have mapped stress changes caused by the Tohoku-oki earthquake but most have considered only 2D maps of stress within a particular plate, and ignored changes with depth (*Hasegawa et al.*, 2011, 2012; *Yoshida et al.*, 2019). *Yang et al.* (2013) produced 3D maps of pre- and post-Tohoku-oki stress, although they had only a short duration catalog available for the post-Tohoki-oki period, and they also incorporate previously modelled coseismic stress changes into their inversion. Here, we divide the available earthquake focal mechanisms into those pre- and post-Tohoku-oki and we produce an independent, 3D assessment of stress for each time period. We include only earthquakes >6 months after the mainshock in the post-Tohoku-oki group, so in addition to coseismic slip stress changes may also incorporate cumulative effects of afterslip and aftershocks, including triggered earthquake swarms in the forearc (*Yoshida et al.*, 2019).

Example maps and cross-sections are shown in Figures 6–9. For comparison, Figure 10 displays a slip model of the Tohoku-oki earthquake. Note that although the stress inversions extend over 200 km offshore, stress estimates in the far offshore (particularly where the distance to shore exceeds focal depth) should be interpreted more cautiously because of much greater uncertainties on focal depths (*Nakamura et al.*, 2016; *Wang et al.*, 2019). Focal depth uncertainties, which are not accounted for in the estimates of stress uncertainty, likely blur the stress tensors over ±20 km depth and prevent us from observing detailed stress patterns around the shallow plate interface. However, we observe such substantial stress rotation between the pre- and post-Tohoku-oki periods, both near the megathrust rupture area and more landward, that they can be interpreted in broad terms without depth blurring being a major concern. Although the changes can be observed by visually comparing the pre- and post-Tohoku-oki maps and cross-sections, to simplify interpretation we also estimate a rotation angle between the two stress states. Similarly to how we defined U (Eq. 3), we consider R in computing meaningful estimates of stress rotation. For uniaxial compression ($R \rightarrow 1$), the estimate of stress rotation should focus on σ_1, whereas for uniaxial extension ($R \rightarrow 0$), rotation estimates should focus on σ_3. Noting that R will also vary between the two stress states, we define the stress rotation ϕ as:

$$\phi = \bar{R}\Delta\overrightarrow{\sigma_1} + (1 - \bar{R})\Delta\overrightarrow{\sigma_3}, \tag{4}$$

where $\bar{R}$ is the mean of the pre- and post-rotation R values. This definition has an issue in that the maximum possible ϕ is 90°, whereas the maximum rotation possible between two general stress tensors is 120°, but it avoids artificially high rotation angles due to, e.g. high $\Delta\overrightarrow{\sigma_3}$ for an area where R is near 1. Resulting ϕ are shown in map view (Figure 11) and cross-sections (Figure 12).

Line E is at the southern end of the area of highest slip (Figure 10) and has the most dramatic stress rotations, which are best viewed in cross-section (Figure 8). Rotations are near 90° even at $x = 160$ km, where the plate interface is at 35–40 km depth. Figure 6 displays near-horizontal σ_1 pre-Tohoku-oki in this region, and near vertical σ_1 afterwards. The along-strike range over which we observe the most significant rotations is consistent with previous observations (*Hasegawa et al.*, 2012) and modelling (*Yang et al.*, 2013; *Wang et al.*, 2019), although the degree of rotation we observe is often higher than predicted by those models. This may indicate that weaker faults and lower differential stress exist in the forearc than typically assumed. We expect that Line D, which traverses the northern end of the highest-slip area, would display similarly large stress rotations if not for the fact that there are so few post-Tohoku-oki forearc earthquakes in the area.

There are also crustal areas of onshore Japan that see significant stress rotation between the pre- and post-Tohoku-oki periods, such as near 40°N, 141°E, on Lines C and D (Figures 6, 11, and 12). These changes may be related to the Tohoku-oki earthquake, though less directly, via fluid upwelling and associated earthquake swarms promoted by the coseismic stress change (margin-normal extension) in this region (*Terakawa et al.*, 2013; *Yoshida et al.*, 2019).

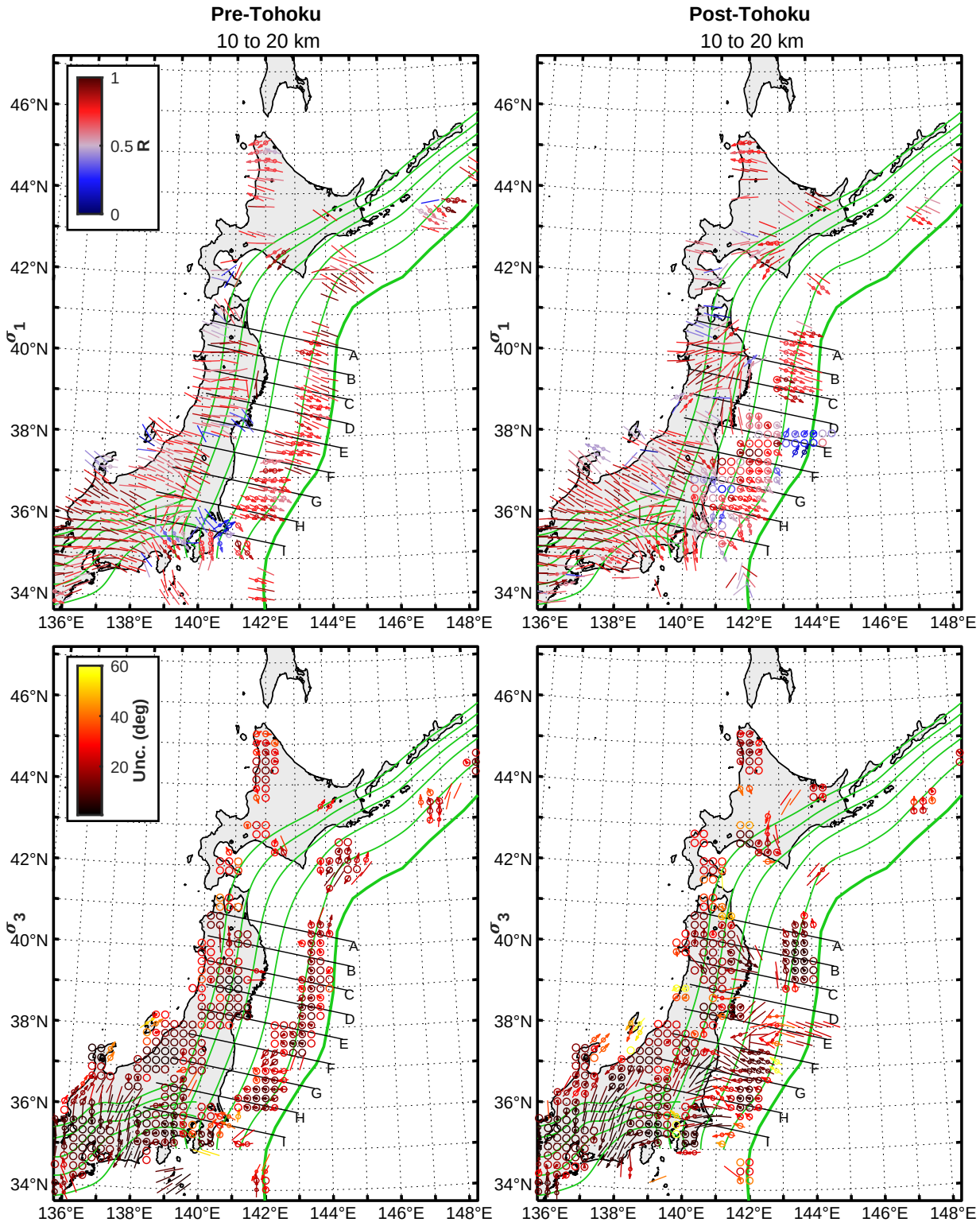

Figure 6. Stress in northern Japan at 10–20 km depth for the (left) pre- and (right) post-Tohoku-oki periods. Top panels display σ_1 and bottom panels display σ_3. The thick green line indicates the trench, and the thin green lines indicate the 20, 40, 60, 80, and 100 km plate-interface contours of *Hayes et al.* (2018). Lines labeled A–I indicate cross-section locations, and are each 400 km long.

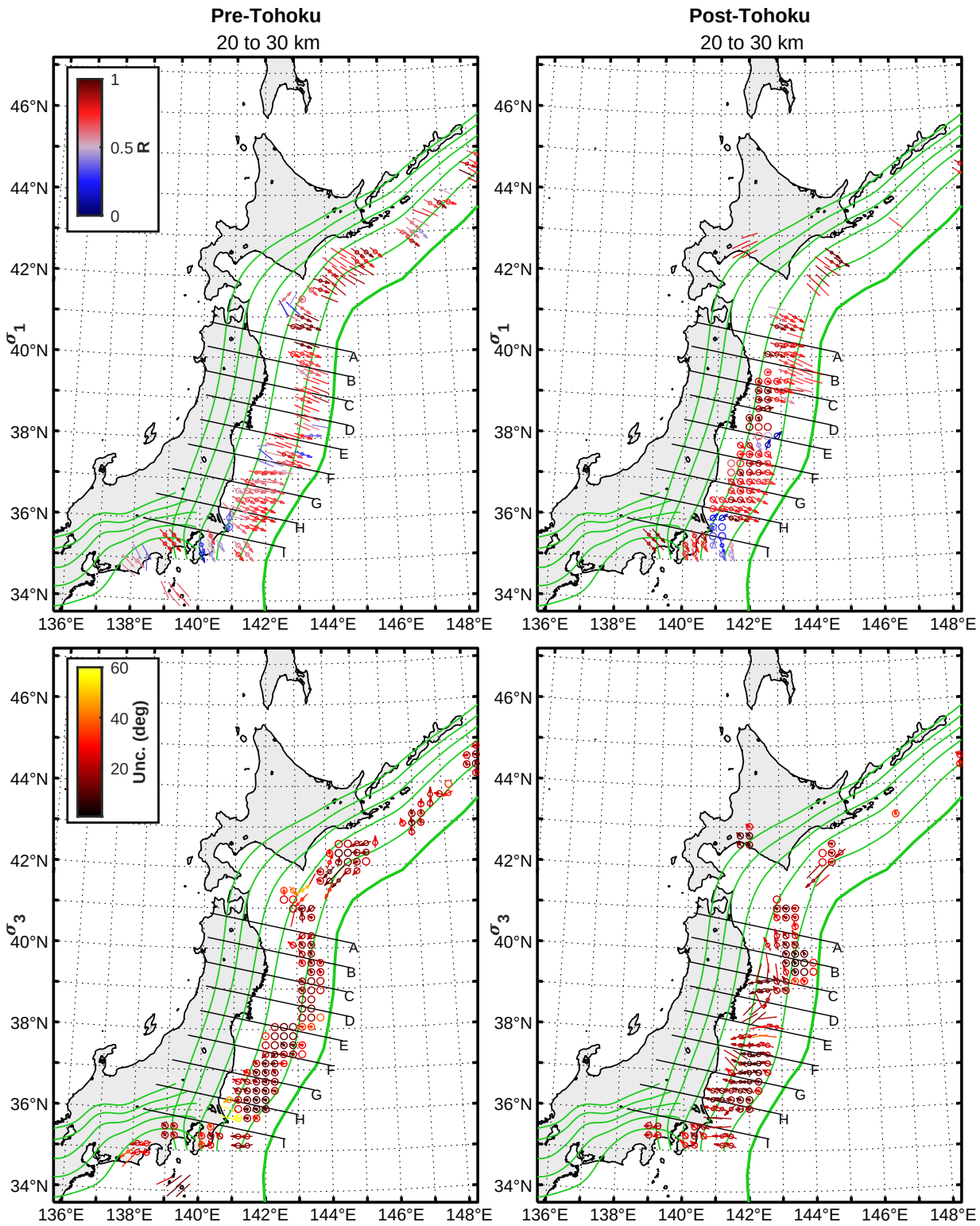

Figure 7. Stress in northern Japan at 20–30 km depth for the (left) pre- and (right) post-Tohoku-oki periods. Top panels display σ_1 and bottom panels display σ_3. Lines labeled A–I indicate cross-section locations, and are each 400 km long. Note that in the northern section of the Tohoku-Oki rupture zone (near lines A–D), pre-Tohoku-Oki earthquakes are primarily in the slab whereas post-Tohoku-oki earthquakes are primarily in the forearc.

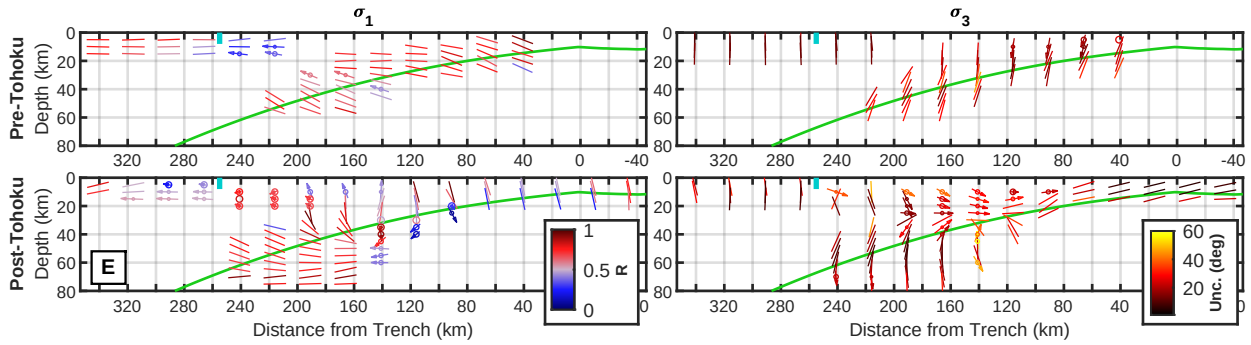

Figure 8. Cross-sections of stress in northern Japan at on Line E (see Figures 6, 7) for the (top) pre- and (bottom) post-Tohoku-oki periods. Cyan markers at the surface indicate the position of the coastline in each section.

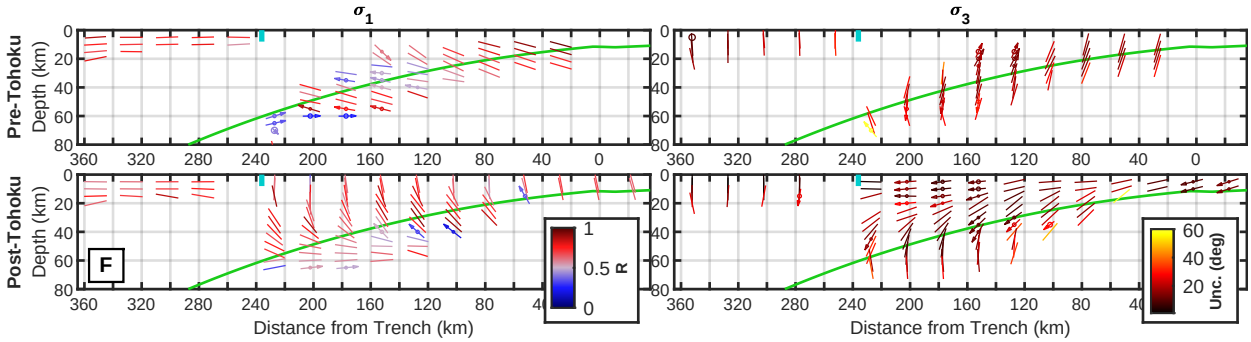

Figure 9. Cross-sections of stress in northern Japan at on Line F (see Figures 6, 7) for the (top) pre- and (bottom) post-Tohoku-oki periods. Cyan markers at the surface indicate the position of the coastline in each section.

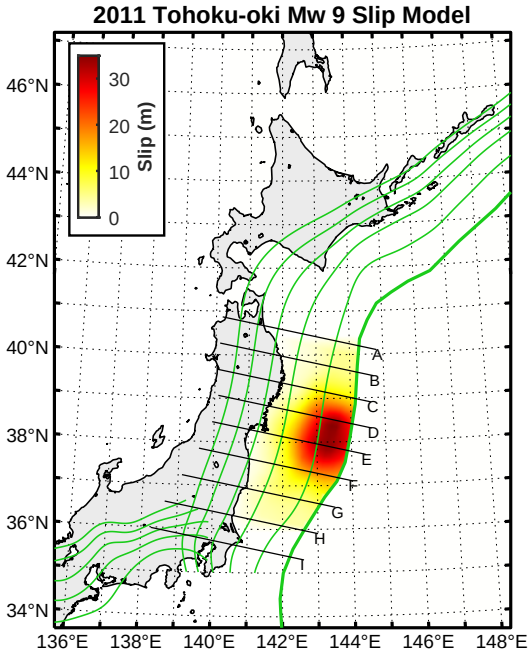

Figure 10. Coseismic slip model of the 2011 Tohoku-oki earthquake from *Wang et al.* (2018). The model is the mean of 44 published coseismic slip models compiled by *Sun et al.* (2017), plus that of *Freed et al.* (2017).

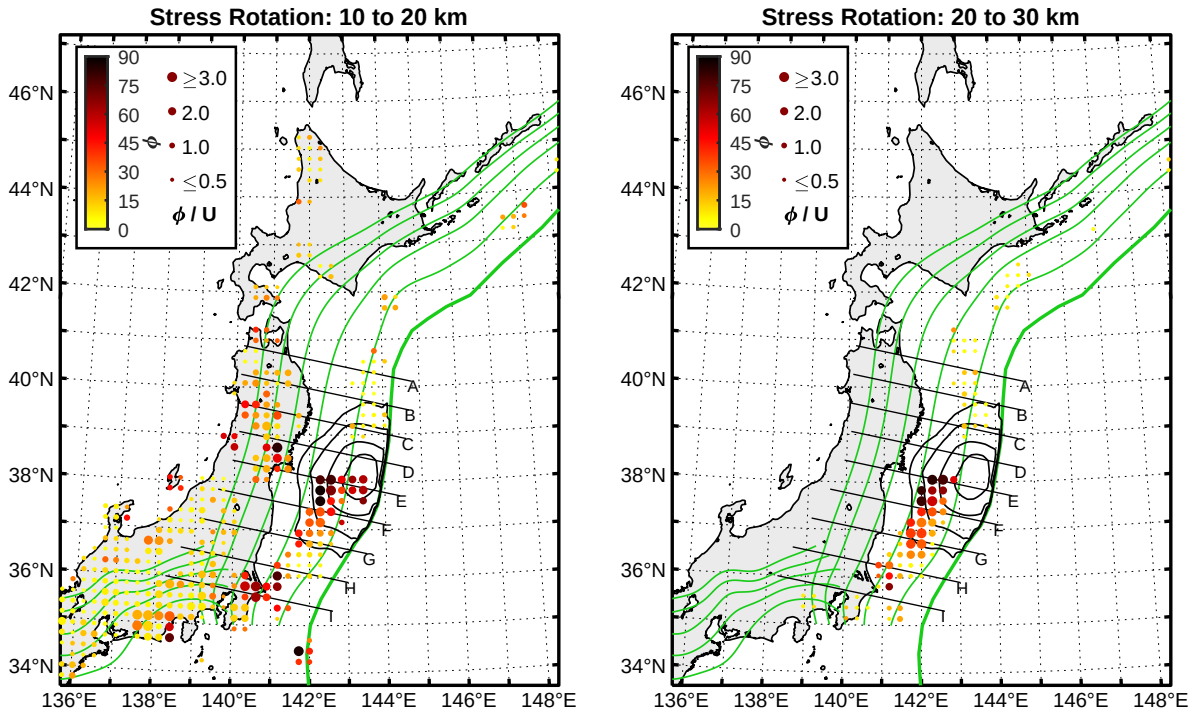

Figure 11. Angle of rotation ϕ, as defined by Eq. 4 between the pre- and post-Tohoku-oki datasets for the (left) 10–20 km and (right) 20–30 km depth intervals. Markers are colored according to ϕ and scaled according to the $\phi/\bar{U}$, where $\bar{U}$ is the mean uncertainty angle of the pre- and post-Tohoku-oki inversions at that grid point. Lines labeled A–I indicate cross-section locations, and are each 400 km long. Black curves show the 5, 10, 20, and 30 m slip contours of the Tohoku-oki earthquake from *Wang et al.* (2018).

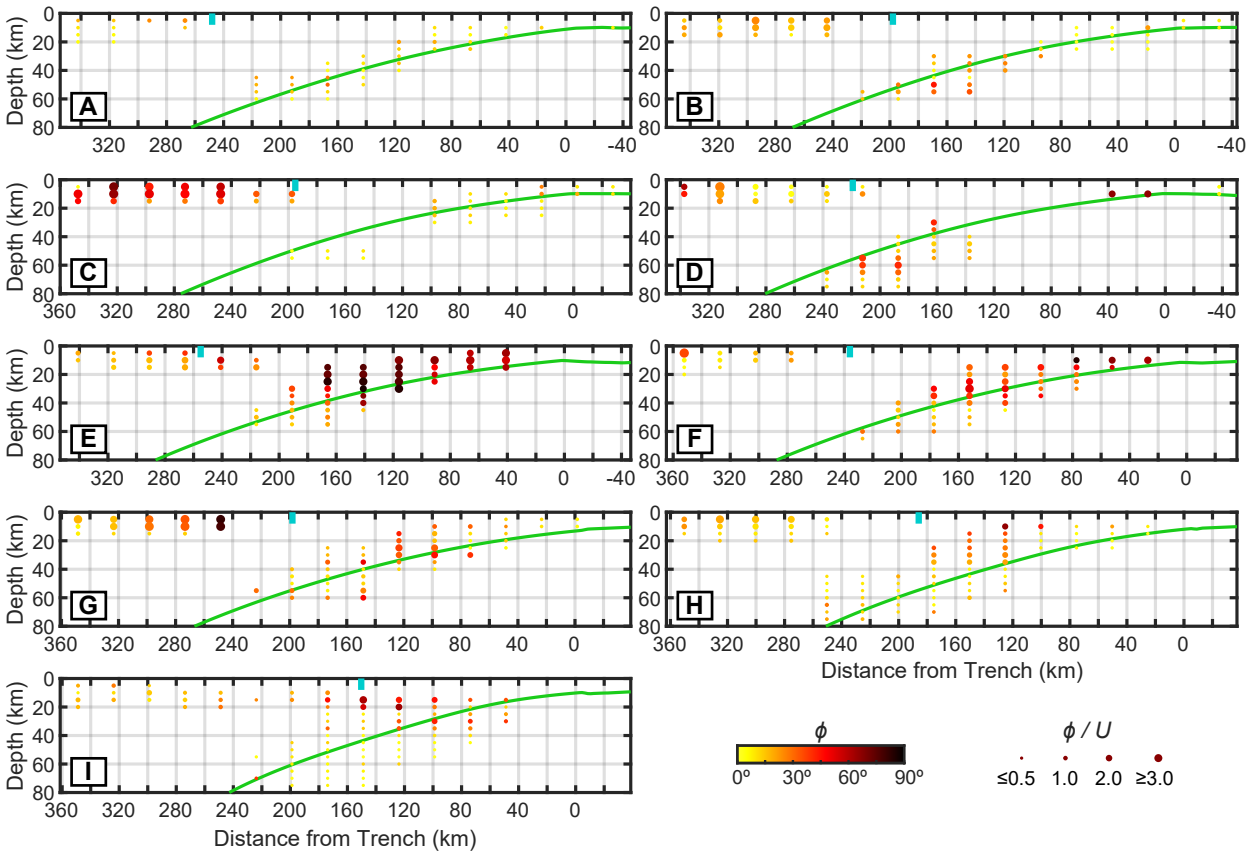

Figure 12. Cross-section views of ϕ, see Figure 11 for locations. Cyan markers at the surface indicate the position of the coastline in each section.

3.4 Southern Japan

Some of the Nankai subduction zone in southern Japan may also be in a "post-seismic" phase following relatively recent megathrust ruptures: the 1944 Showa Tonankai M 8.1 and the 1946 Showa Nankai M 8.3 earthquakes, which are reviewed by *Okamura and Shishikura* (2020). The combined along-strike extent of these ruptures spans approximately from Line B to Line E on our stress maps (Figure 13). Above the rupture zones there are many gaps where stress could not be resolved due to a lack of seismicity; however, on Lines B–D forearc σ_1 is margin-parallel near the coastline, whereas it is closer to margin-normal outside the rupture zones, on Lines A and F (Figure 14). Far to the southwest on Lines H–I, which intersect an extensional back-arc (Figure 13), σ_1 in the shallow crust is near-vertical even in the offshore forearc, although at $\gtrsim$20 km depth there is a compressive stress regime that appears to be continuous across the plate interface.

On all cross-sections with forearc stress inversions both above and below $\sim$20 km depth, there is strong evidence for a stress rotation with depth. This is most apparent on Line F, where there is a substantial rotation at $\sim$20 km depth, and where the deeper stress state is compressive and continuous across the plate

interface. Similar patterns are observed on Lines B, E, and G–J, although on Lines G–J the stress contrast with depth is visible only offshore, and occurs at shallower depths. On Lines E and F this stress state is observed up to ∼30 km shallower than the plate interface model, so it is unlikely that the stress contrast is in fact near the plate interface, even if there are high errors in focal depths and/or interface depth.

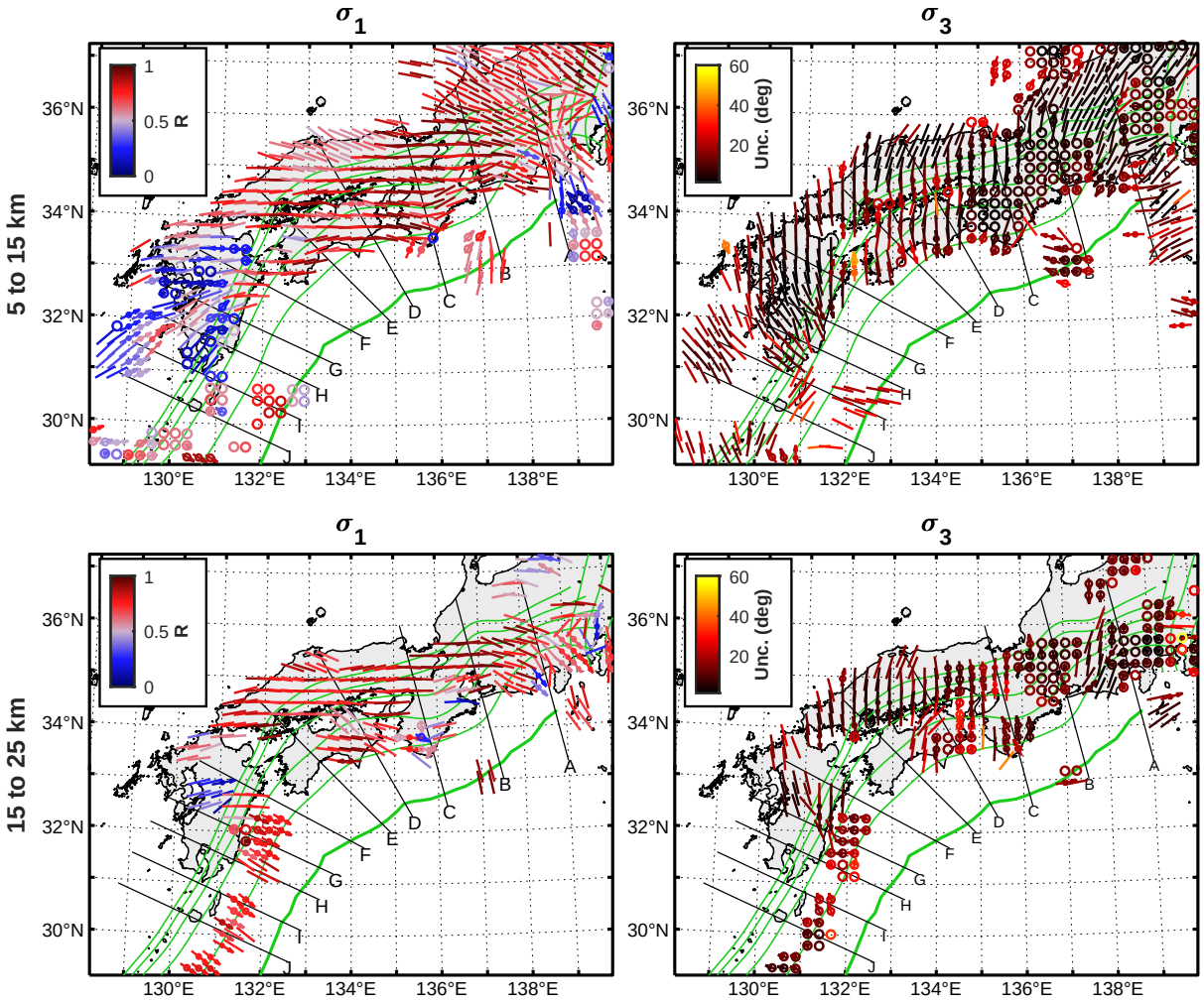

Figure 13. Stress inversion results from the Nankai Subduction Zone, southern Japan for the (top) 5–15 km and (bottom) 15–25 km depth ranges. The thick green line indicates the trench, and the thin green lines indicate the 20, 40, 60, 80, and 100 km plate-interface contours of *Hayes et al.* (2018). Lines labeled A–J indicate cross-section locations, and are each 400 km long.

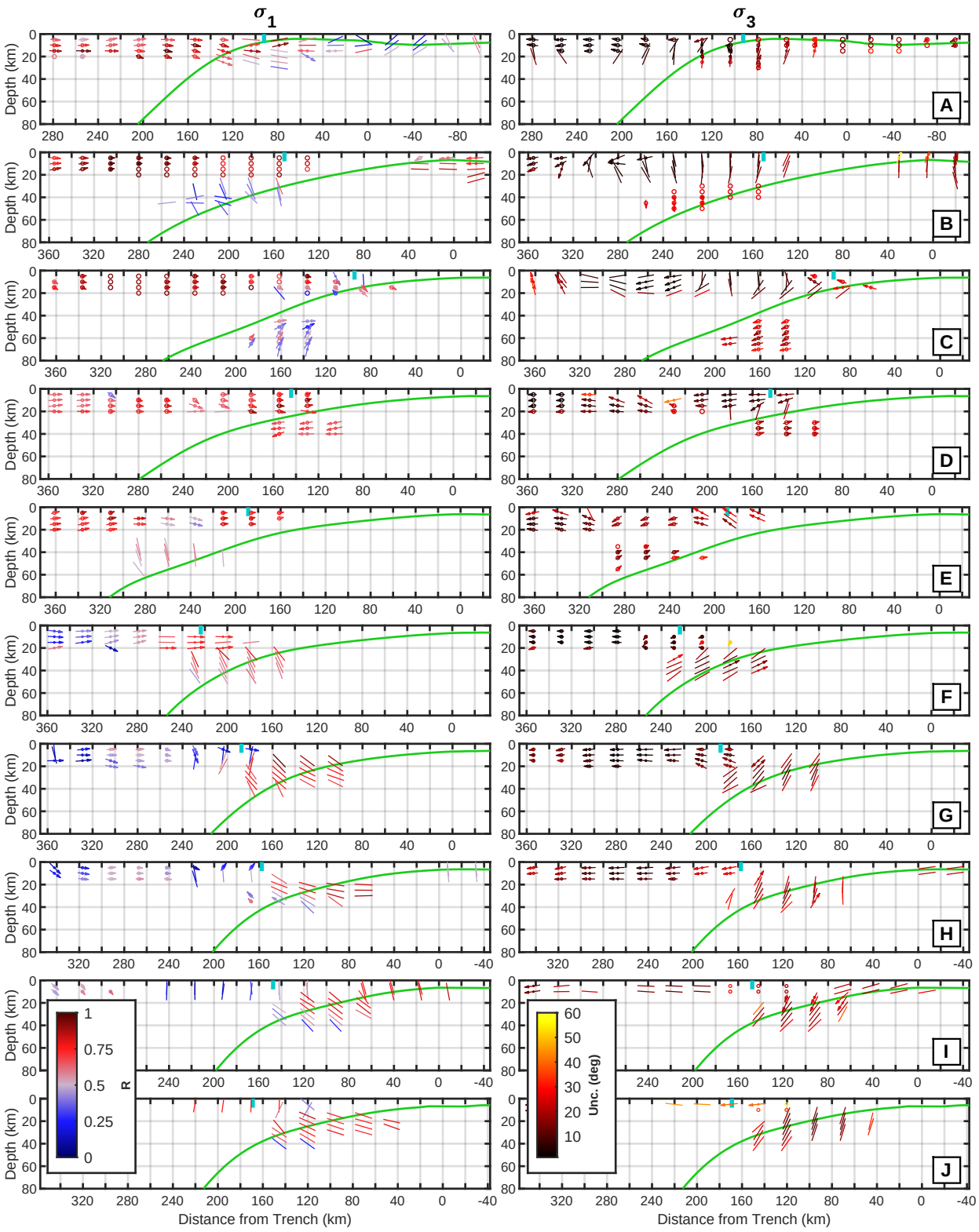

Figure 14. Cross-sections of stress in southern Japan, see Figure 13 for locations. Cyan markers at the surface indicate the position of the coastline in each section.

3.5 Mexico

The Mexican Subduction Zone, where the subducting Cocos plate collides with North America, has produced megathrust earthquakes at least as large as $M_W \sim 8.6$ (*Suárez and Albini*, 2009), but more commonly ruptures in smaller M_W 7–8 earthquakes. A region termed the Guerrero Seismic Gap (GSG), spanning approximately 101.2°W–100.2°W (or 101.2°W–99.2°W for the extended GSG), is exceptional in that it has not had a significant megathrust earthquake since 1911. Although the GSG has had recent large slow slip events, the estimated slip deficit remain substantial (*Bekaert et al.*, 2015; *Cruz-Atienza et al.*, 2018).

We resolve stress mainly near the the shallow, locked portion of the subduction zone, offshore and just onshore, where the stress field appears to be dominated margin-normal compression (Figure 15). This is true in both the subducting and overriding plate (although we remain cautious of blurring along depth, especially offshore), with the exception of in Line B, where there is a rotation from near-horizontal σ_1 in the subducting plate to steeply seaward-dipping σ_1 in the forearc (Figure 16). Line B falls in the western portion of the GSG, so this may be reflective of anomalously low coupling in the region. Line C falls just east of the GSG; there are unfortunately insufficient data to resolve forearc stress in the eastern (extended) GSG in order to see if the stress rotation is present there.

Lines A and B each contain a region with stress inversions of deeper, intraslab seismicity. The two regions show opposite stress regimes; Line A shows along-dip extension whereas Line B, whose inversions are relatively close to the trench, shows along dip compression. Although there are too few focal mechanisms farther than ∼60 km inland to formally invert from stress, near the NE end of Line B *Pacheco and Singh* (2010) note two normal-faulting mechanisms with strikes near-parallel to the coast, suggestive of trench-normal extension.

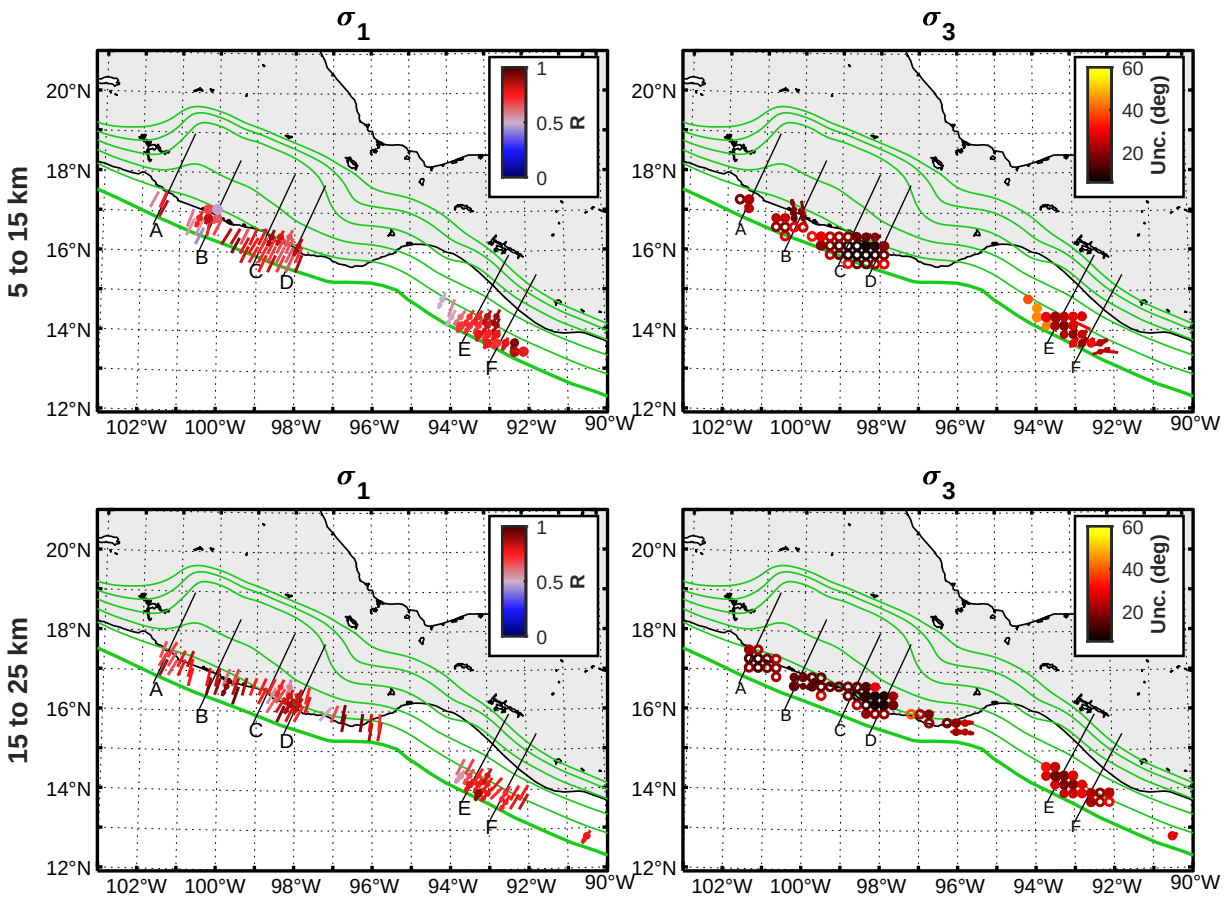

Figure 15. Stress inversion results from the Mexican Subduction Zone for the (top) 5–15 km and (bottom) 15–25 km depth ranges. The thick green line indicates the trench, and the thin green lines indicate the 20, 40, 60, 80, and 100 km plate-interface contours of *Hayes et al.* (2018). Lines labeled A–F indicate cross-section locations, and are each 280 km long.

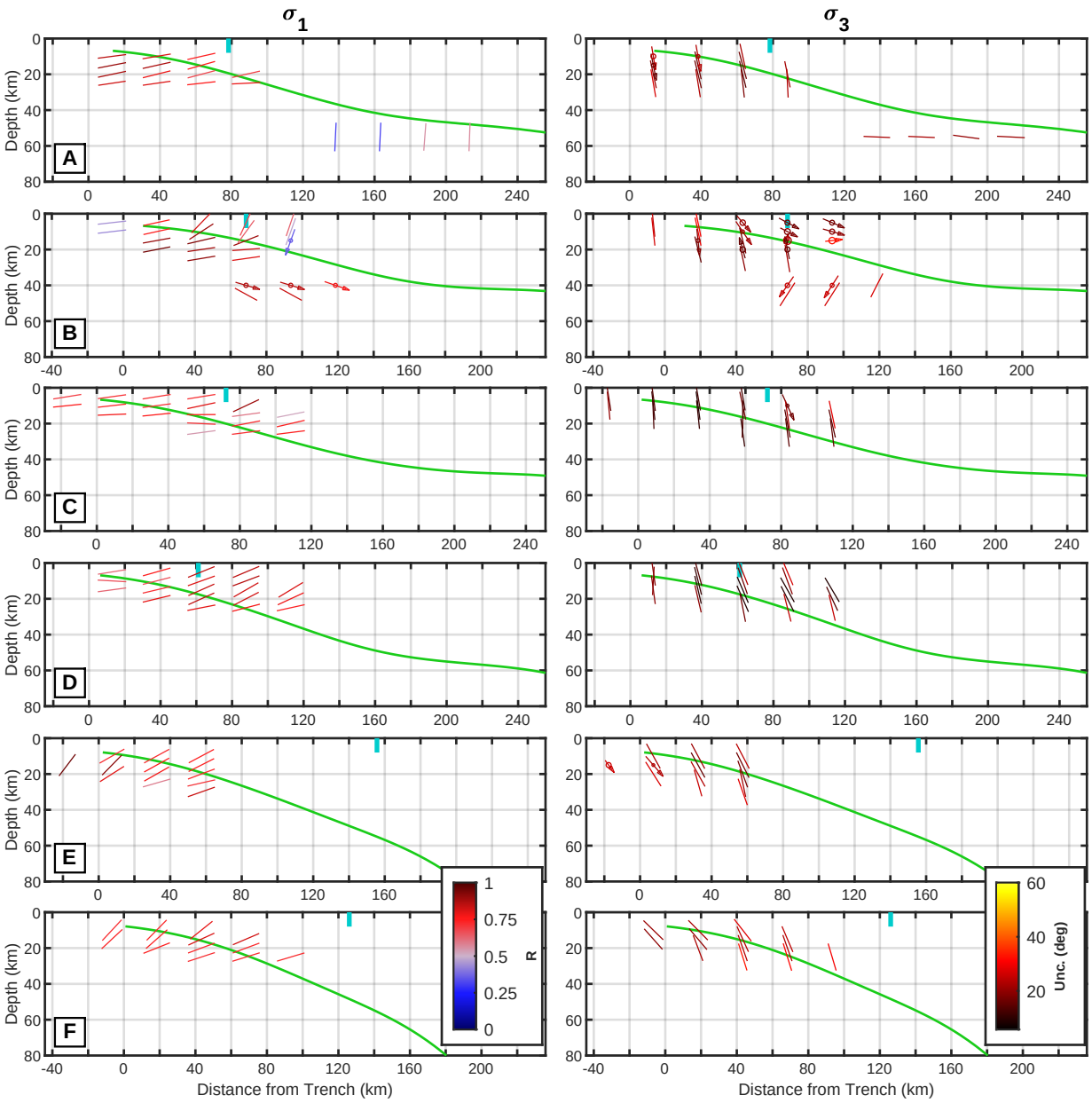

Figure 16. Cross-sections of stress in Mexico, see Figure 15 for locations. Cyan markers at the surface indicate the position of the coastline in each section.

3.6 Northern Chile

Herrera et al. (2021) computed 817 focal mechanisms from the northern Chile forearc, divided them into five groups based on epicentral location, and inverted each group for a stress tensor. They observed a rotation from margin-parallel compression near the coast to margin-normal compression further inland. We observe the same trend here; in Figure 17 the margin-normal regime is seen in only a single stress tensor (in the 15–25 km depth interval, near 21°S, 69°W), but it is more extensively resolved at shallower depths and is visible in the cross-section of Line E (Figure 18). In this work we also include focal mechanisms from ISC Bulletin, which are predominantly offshore, both in the forearc and the subducting plate. Similar to Cascadia, σ_1 is consistently margin-normal offshore (above the shallow, locked interface), usually dipping moderately to the west, and σ_3 is always near-vertical. R varies substantially offshore, with a low-R region of forearc (relatively equal margin-parallel and -normal compression) in between high-R regions (dominated by margin-normal compression) to the north and south. The transition point to the (onshore) margin-normal compression regime appears to be $\sim$30 km west (seaward) of the coastline on Lines A and B, but much closer to the coastline on Lines C and D.

We resolve no significant changes of stress with depth in the offshore or nearshore regions. However, in the far-inland region where there is near–margin-normal compression (east of 69.2°W, Line E), there is a rotation from ENE-trending σ_1 in the 0–15 km depth range to NW-trending, more steeply dipping σ_1 from 30–45 km. Stress is not resolved in the 15–30 km depth range so it is unclear if there is a sharp or gradual transition between these regimes.

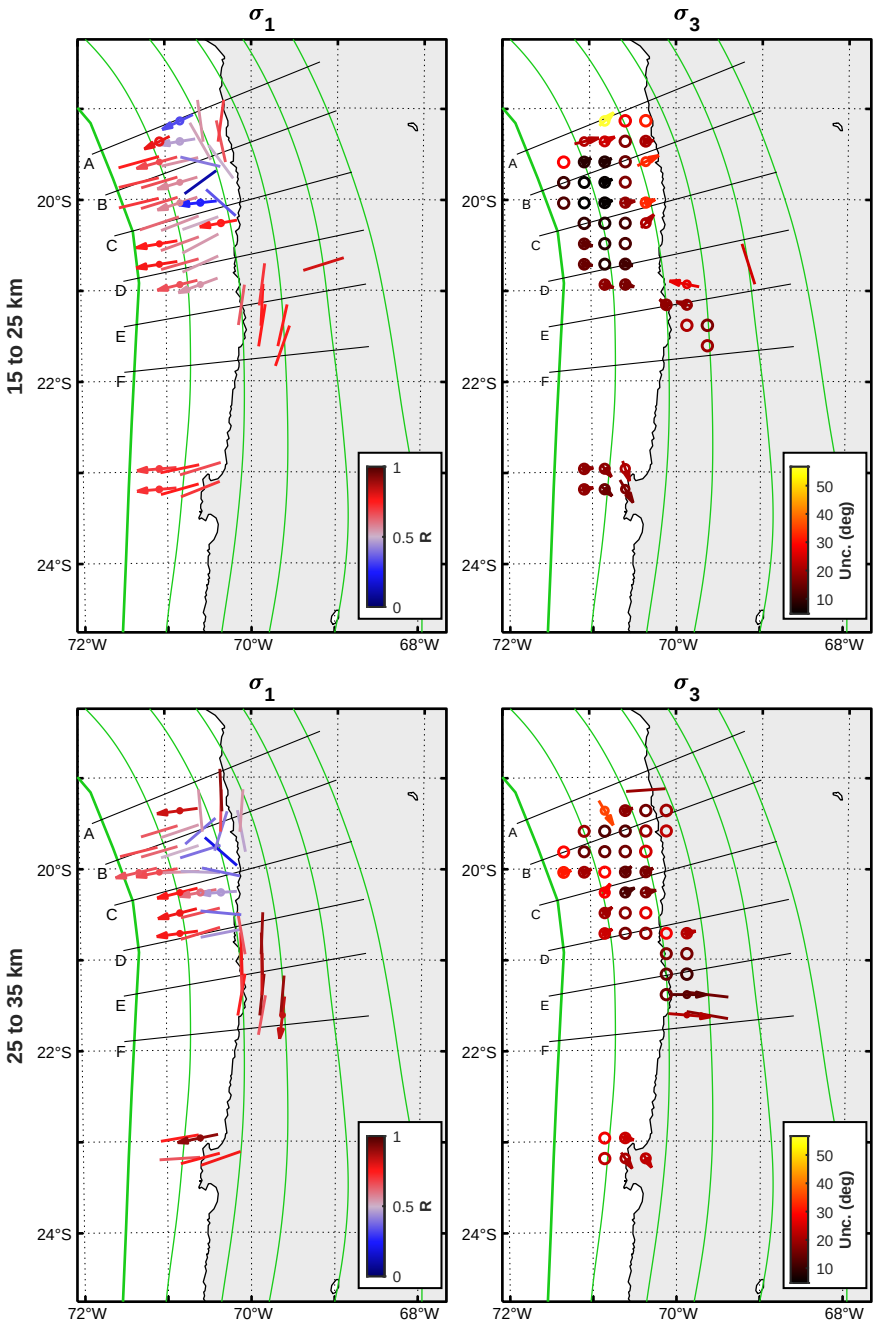

Figure 17. Stress inversion results from northern Chile for the (top) 15–25 km and (bottom) 25–35 km depth ranges. The thick green line indicates the trench, and the thin green lines indicate the 20, 40, 60, 80, and 100 km plate-interface contours of *Hayes et al.* (2018). Lines labeled A–F indicate cross-section locations, and are each 300 km long.

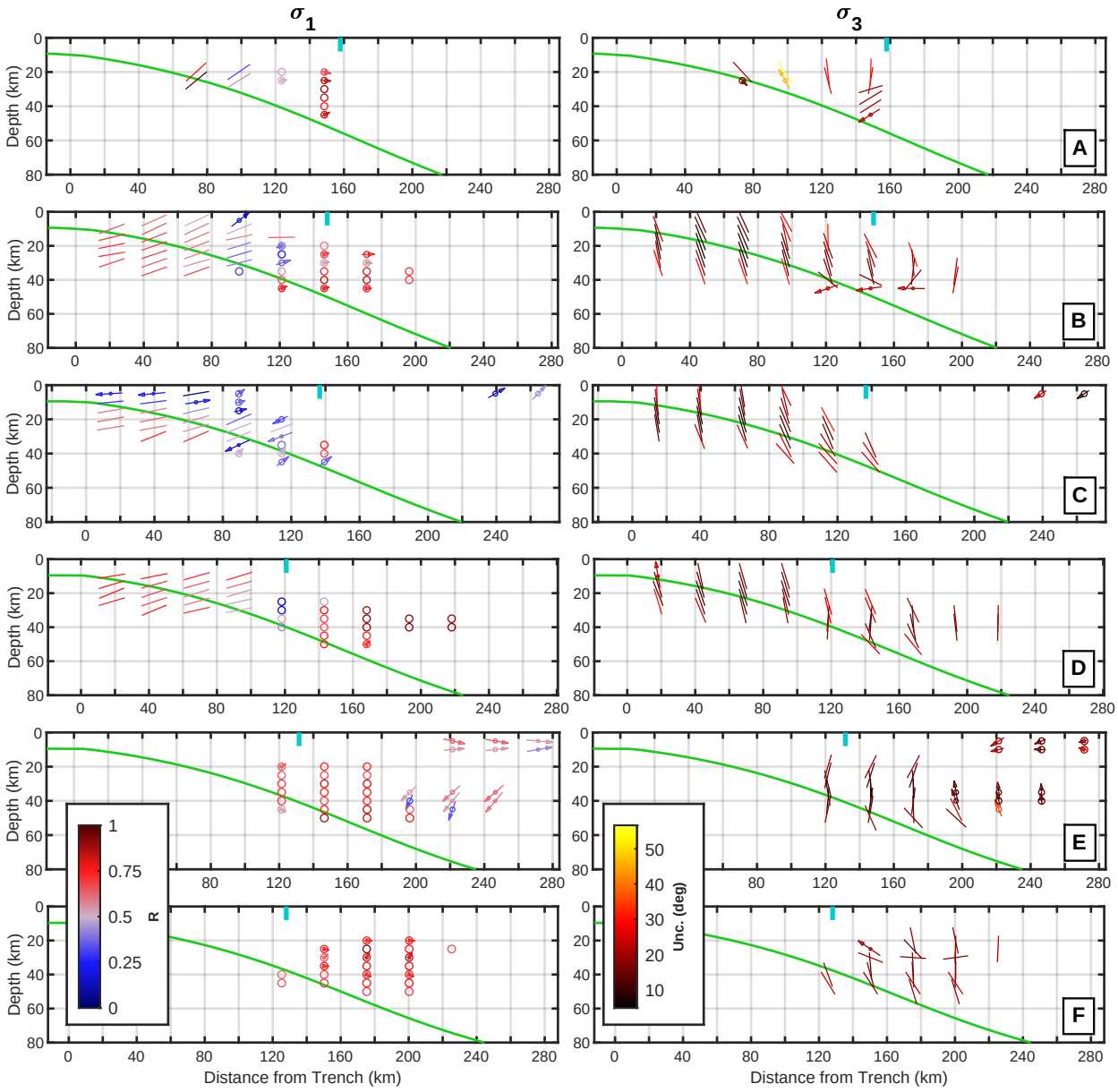

Figure 18. Cross-sections of stress in northern Chile, see Figure 17 for locations. Cyan markers at the surface indicate the position of the coastline in each section.

4 Discussion and Conclusions

We computed 181380 stress inversions across five subduction zones, providing the first examination of along-depth stress variation from focal mechanisms for those outside of Japan. Our results, along with a recent study in eastern Canada (*Plourde and Nedimović*, 2021), indicate that substantial along-depth variations in the tectonic stress tensor appear to be common in the middle to lower crust. Interpreting the observed changes with depth, like interpretation of focal-mechanism derived stress patterns in general, is challenging due in part to the lack of information on the scale of differential stress. Our results, for example, do not indicate whether a $\sim 90^{\circ}$ rotation in stress, either in time or space, reflects a difference on the order of 0.1 MPa or 10 MPa. However, it seems most plausible that the major stress rotations that we observe, including those in time (in the Japan forearc) and depth (in the Cascadia and Nankai forearcs), represent small changes in absolute stress levels in areas of relatively low differential stress. This is consistent with studies such as *Bostock et al.* (2019) and *Sibson* (2020) that suggest pore-fluid pressure, via its influence on effective normal stress, is critical in controlling earthquake distributions in forearcs. Rheological and/or compositional discontinuities in the forearc, potentially correlating with observations such as the reported Conrad discontinuity in Nankai (*Katsumata*, 2010), could also contribute to dramatic stress rotation over short depth intervals. Interpreting 3D stress patterns with confidence will require context from geodynamic models tailored to each specific subduction zone, and is largely beyond the scope of this study. In the future, these observations will contribute to geodynamic models of subduction zones and further our understanding of the hazard posed by megathrust earthquakes and tsunamis.

References

Balfour NJ, Cassidy JF, Dosso SE, and Mazzotti S. [2011]. Mapping crustal stress and strain in southwest british columbia. *Journal of Geophysical Research: Solid Earth*, 116, doi:10.1029/2010JB008003.

Bekaert DPS, Hooper A, and Wright TJ. [2015]. Reassessing the 2006 Guerrero slow-slip event, Mexico: Implications for large earthquakes in the Guerrero Gap. *Journal of Geophysical Research: Solid Earth*, 120, 1357–1375, doi:10.1002/2014JB011557.

Bostock MG, Christensen NI, and Peacock SM. [2019]. Seismicity in cascadia. *Lithos*, 332–333, 55–66, doi:10.1016/j.lithos.2019.02.019.

Cruz-Atienza VM, Ito Y, Kostoglodov V, Hjörleifsdóttir V, Iglesias A, Tago J, Calò M, Real J, Husker A, Ide S, Nishimura T, Shinohara M, Mortera-Gutierrez C, García S, and Kido M. [2018]. A seismogeodetic amphibious network in the Guerrero Seismic Gap, Mexico. *Seismological Research Letters*, 89, 1435–1449, doi:10.1785/0220170173.

Dziewonski AM, Chou TA, and Woodhouse JH. [1981]. Determination of earthquake source parameters from waveform data for studies of global and regional seismicity. *Journal of Geophysical Research: Solid Earth*, 86, 2825–2852, doi:10.1029/JB086iB04p02825.

Ekström G, Nettles M, and Dziewoński A. [2012]. The global cmt project 2004–2010: Centroid-moment tensors for 13,017 earthquakes. *Physics of the Earth and Planetary Interiors*, 200-201, 1–9, doi:10.1016/j.pepi.2012.04.002.

Franco SI, Iglesias A, and Fukuyama E. [2020]. Moment tensor catalog for Mexican earthquakes: almost two decades of seismicity. *Geofísica Internacional*, 59, 54–80.

Freed AM, Hashima A, Becker TW, Okaya DA, Sato H, and Hatanaka Y. [2017]. Resolving depth-dependent subduction zone viscosity and afterslip from postseismic displacements following the 2011 Tohoku-oki, Japan earthquake. *Earth and Planetary Science Letters*, 459, 279–290, doi:10.1016/j.epsl.2016.11.040.

Hasegawa A, Yoshida K, and Okada T. [2011]. Nearly complete stress drop in the 2011 M w 9.0 off the Pacific coast of Tohoku Earthquake. *Earth, Planets and Space*, 63, 703–707, doi:10.5047/eps.2011.06.007.

Hasegawa A, Yoshida K, Asano Y, Okada T, Iinuma T, and Ito Y. [2012]. Change in stress field after the 2011 great tohoku-oki earthquake. *Earth and Planetary Science Letters*, 355-356, 231–243, doi:10.1016/j.epsl.2012.08.042.

Hayes GP, Moore GL, Portner DE, Hearne M, Flamme H, Furtney M, and Smoczyk GM. [2018]. Slab2, a comprehensive subduction zone geometry model. *Science*, 362, 58–61, doi:10.1126/science.aat4723.

Heidbach O, Rajabi M, Cui X, Fuchs K, Müller B, Reinecker J, Reiter K, Tingay M, Wenzel F, Xie F, Ziegler MO, Zoback ML, and Zoback M. [2018]. The world stress map database release 2016: Crustal stress pattern across scales. *Tectonophysics*, 744, 484–498, doi:10.1016/j.tecto.2018.07.007.

Herrera C, Cassidy JF, Dosso SE, Dettmer J, Bloch W, Sippl C, and Salazar P. [2021]. The crustal stress field inferred from focal mechanisms in northern Chile. *Geophysical Research Letters*, 48, e2021GL092889, doi:10.1029/2021GL092889.

Kagan YY. [2007]. Simplified algorithms for calculating double-couple rotation. *Geophysical Journal International*, 171, 411–418, doi:10.1111/j.1365-246X.2007.03538.x.

Katsumata A. [2010]. Depth of the Moho discontinuity beneath the Japanese islands estimated by traveltime analysis. *Journal of Geophysical Research: Solid Earth*, 115, B005864, doi:10.1029/2008JB005864.

Lentas K, Di Giacomo D, Harris J, and Storchak DA. [2019]. The ISC Bulletin as a comprehensive source of earthquake source mechanisms. *Earth System Science Data*, 11, 565–578, doi:10.5194/essd-11-565-2019.

Li D, McGuire JJ, Liu Y, and Hardebeck JL. [2018]. Stress rotation across the Cascadia megathrust requires a weak subduction plate boundary at seismogenic depths. *Earth and Planetary Science Letters*, 485, 55–64, doi:10.1016/j.epsl.2018.01.002.

Lund B and Slunga R. [1999]. Stress tensor inversion using detailed microearthquake information and stability constraints: Application to Ölfus in southwest iceland. *Journal of Geophysical Research: Solid Earth*, 104, 14947–14964, doi:10.1029/1999JB900111.

Mazzotti S and Townend J. [2010]. State of stress in central and eastern North American seismic zones. *Lithosphere*, 2, 76–83, doi:10.1130/L65.1.

McCaffrey R, King RW, Payne SJ, and Lancaster M. [2013]. Active tectonics of northwestern U.S. inferred from GPS-derived surface velocities. *Journal of Geophysical Research: Solid Earth*, 118, 709–723, doi:10.1029/2012JB009473.

McCrory PA, Blair JL, Waldhauser F, and Oppenheimer DH. [2012]. Juan de Fuca slab geometry

and its relation to Wadati-Benioff zone seismicity. *Journal of Geophysical Research*, 117, B09306, doi:10.1029/2012JB009407.

Michael AJ. [1984]. Determination of stress from slip data: Faults and folds. *Journal of Geophysical Research: Solid Earth*, 89, 11517–11526, doi:10.1029/JB089iB13p11517.

Nakamura W, Uchida N, and Matsuzawa T. [2016]. Spatial distribution of the faulting types of small earthquakes around the 2011 tohoku-oki earthquake: A comprehensive search using template events. *Journal of Geophysical Research: Solid Earth*, 121, 2591–2607, doi:10.1002/2015JB012584.

Okamura Y and Shishikura M. [2020]. New hypothesis to explain Quaternary forearc deformation and the variety of plate boundary earthquakes along the Suruga–Nankai Trough by oblique subduction of undulations on the Philippine Sea Plate. *Earth, Planets and Space*, 72, doi:10.1186/s40623-020-01183-5.

Pacheco JF and Singh SK. [2010]. Seismicity and state of stress in Guerrero segment of the Mexican subduction zone. *Journal of Geophysical Research: Solid Earth*, 115, B006453, doi:10.1029/2009JB006453.

Plourde AP and Bostock MG. [2019]. Relative moment tensors and deep Yakutat seismicity. *Geophysical Journal International*, 219, 1447–1462, doi:10.1093/gji/ggz375.

Plourde AP and Nedimović MR. [2021]. Earthquake depths, focal mechanisms, and stress in the Lower St. Lawrence Seismic Zone. *Seismological Research Letters*, 92, 2562–2572, doi:10.1785/0220200429.

Sibson RH. [2020]. Dual-driven fault failure in the lower seismogenic zone. *Bulletin of the Seismological Society of America*, , doi:10.1785/0120190190.

Suárez G and Albini P. [2009]. Evidence for great tsunamigenic earthquakes (M 8.6) along the Mexican Subduction Zone. *Bulletin of the Seismological Society of America*, 99, 892–896, doi:10.1785/0120080201.

Sun T, Wang K, Fujiwara T, Kodaira S, and He J. [2017]. Large fault slip peaking at trench in the 2011 Tohoku-oki earthquake. *Nature communications*, 8, 1–8, doi:10.1038/ncomms14044.

Terakawa T and Matsu'ura M. [2010]. The 3-D tectonic stress fields in and around Japan inverted from centroid moment tensor data of seismic events. *Tectonics*, 29, TC6008, doi:10.1029/2009TC002626.

Terakawa T, Hashimoto C, and Matsu'ura M. [2013]. Changes in seismic activity following the 2011 tohoku-oki earthquake: Effects of pore fluid pressure. *Earth and Planetary Science Letters*, 365, 17–24, doi:10.1016/j.epsl.2013.01.017.

Uchide T. [2020]. Focal mechanisms of small earthquakes beneath the Japanese islands based on first-motion polarities picked using deep learning. *Geophysical Journal International*, 223, 1658–1671, doi:10.1093/gji/ggaa401.

Vavryčuk V. [2014]. Iterative joint inversion for stress and fault orientations from focal mechanisms. *Geophysical Journal International*, 199, 69–77, doi:10.1093/gji/ggu224.

Wada I, Mazzotti S, and Wang K. [2010]. Intraslab stresses in the Cascadia Subduction Zone from inversion of earthquake focal mechanisms. *Bulletin of the Seismological Society of America*, 100, 2002–2013, doi:10.1785/0120090349.

Wang K, Sun T, Brown L, Hino R, Tomita F, Kido M, Iinuma T, Kodaira S, and Fujiwara T. [2018]. Learning from crustal deformation associated with the M9 2011 Tohoku-oki earthquake. *Geosphere*, 14, 552–571, doi:10.1130/GES01531.1.

Wang K, Brown L, Hu Y, Yoshida K, He J, and Sun T. [2019]. Stable forearc stressed by a weak megathrust: mechanical and geodynamic implications of stress changes caused by the M = 9 Tohoku-Oki earthquake. *Journal of Geophysical Research: Solid Earth*, 124, 6179–6194, doi:10.1029/2018JB017043.

Yang YR, Johnson KM, and Chuang RY. [2013]. Inversion for absolute deviatoric crustal stress using focal mechanisms and coseismic stress changes: The 2011 m9 tohoku-oki, japan, earthquake. *Journal of Geophysical Research: Solid Earth*, 118, 5516–5529, doi:10.1002/jgrb.50389.

Yoshida K, Hasegawa A, Yoshida T, and Matsuzawa T. [2019]. Heterogeneities in stress and strength in Tohoku and its relationship with earthquake sequences triggered by the 2011 M9 Tohoku-Oki earthquake. *Pure and Applied Geophysics*, 176, 1335–1355, doi:10.1007/s00024-018-2073-9.